TU Delft

Delft University of Technology

Document Version
Final published version

Licence
CC BY

Citation (APA)
Mr Kundu, S. K., Shen, T., Betlem, K., Ghatkesar, M. K., Steeneken, P. G., & Widdershoven, F. P. (2026). Multispectral UV Imaging on Capacitive CMOS Arrays Enabled by Solution-Processed Metal-Oxide Nanoparticles. *Advanced Science*, Article e76880. https://doi.org/10.1002/advs.76880

Important note
To cite this publication, please use the final published version (if applicable).
Please check the document version above.

Copyright
In case the licence states “Dutch Copyright Act (Article 25fa)”, this publication was made available Green Open Access via the TU Delft Institutional Repository pursuant to Dutch Copyright Act (Article 25fa, the Taverne amendment). This provision does not affect copyright ownership.
Unless copyright is transferred by contract or statute, it remains with the copyright holder.

Sharing and reuse
Other than for strictly personal use, it is not permitted to download, forward or distribute the text or part of it, without the consent of the author(s) and/or copyright holder(s), unless the work is under an open content license such as Creative Commons.

Takedown policy
Please contact us and provide details if you believe this document breaches copyrights.
We will remove access to the work immediately and investigate your claim.

This work is downloaded from Delft University of Technology.

Check for updates

Advanced Science

ADVANCED SCIENCE Open Access

www.advancedscience.com

RESEARCH ARTICLE OPEN ACCESS

Multispectral UV Imaging on Capacitive CMOS Arrays Enabled by Solution-Processed Metal-Oxide Nanoparticles

Suman Kundu[1,2] | Tao Shen[1,2] | Kai Betlem[1,2] | Murali K. Ghatkesar[2] | Peter G. Steeneken[2] | Frans P. Widdershoven[1,3]

[1]Department of Microelectronics, Faculty of Electrical Engineering, Mathematics and Computer Science, TU Delft, Netherlands | [2]Department of Precision and Microsystems Engineering, Faculty of Mechanical Engineering, TU Delft, Netherlands | [3]NXP Semiconductors, Technology & Operations/CTO Office, Eindhoven, Netherlands

Correspondence: Suman Kundu (S.Kundu@tudelft.nl) | Frans P. Widdershoven (frans.widdershoven@nxp.com)

Received: 28 April 2026 | **Revised:** 2 June 2026 | **Accepted:** 21 July 2026

Keywords: capacitive array | CMOS | metal oxides | multispectral detectors | nanoparticles | UV imagers

ABSTRACT

Ultraviolet (UV) imagers are important for a variety of applications, such as quality inspection in the semiconductor industry, forensics and food quality inspection, but are often costly because they require dedicated semiconductor process flows. Here, an imaging chip is introduced that has been fabricated using standard 40 nm complementary metal-oxide-semiconductor (CMOS) technology. Instead of using a conventional charge-based photodetection principle, the imager uses a capacitive operation principle where UV-light causes capacitance changes via the photodielectric effect in a functionalization layer, which are measured by the underlying CMOS circuitry. This spin-coated or inkjet-printed functionalization layer consists of solution-processed, wide-bandgap, semiconducting metal-oxide nanoparticles, such as ZnO, SnO_2 and Ga_2O_3. Owing to their bandgap-dependent optical absorption, these materials exhibit distinct capacitive responses across UV-A, UV-B, and UV-C spectral regions, thereby enabling band-selective detection and multispectral UV imaging. The sensors exhibit low noise-equivalent powers (17-138 fW $Hz^{-1/2}$) across the UV bands. Unlike conventional silicon CMOS imagers, the present capacitive-CMOS platform is inherently visible-blind, providing selective UV detection. This work positions late-functionalized capacitive-CMOS arrays as a route toward reducing the fabrication complexity of UV imagers, which can lead to their more widespread implementation in consumer and low-volume application-specific products.

1 | Introduction

CMOS image sensors form the backbone of modern imaging technologies, providing low cost, high scalability, and seamless integration with on-chip electronics [1–4], and have revolutionized consumer, industrial, automotive and biomedical applications. Next-generation consumer electronics demand a shift from conventional imaging to enhanced vision-perception, requiring sensors made with uncomplicated fabrication technologies, broad spectral sensitivity, and multispectral data integration [5–14]. However, the detection capability of current CMOS image sensors is intrinsically limited by the operation range of the underlying silicon photodiodes, which sharply decreases in the ultraviolet (UV) and infrared (IR) wavelengths owing to poor quantum efficiency [1–5, 8, 10, 12]. Although CMOS-compatible photodetectors have made significant progress in the visible to short-wave IR regions [8, 9, 11, 15], their performance in the UV domain still lags behind [10]. The accurate and selective detection of UV radiation is of great importance, with applications spanning many domains, from

Murali K. Ghatkesar, Peter G. Steeneken and Frans P. Widdershoven contributed equally to this work.

This is an open access article under the terms of the Creative Commons Attribution License, which permits use, distribution and reproduction in any medium, provided the original work is properly cited.

© 2026 The Author(s). *Advanced Science* published by Wiley-VCH GmbH

quality inspection to food quality monitoring, astronomical and biological imaging, forensic analysis, and currency validation [10, 16–20]. Several approaches have been explored to extend CMOS photodetectors into the UV and to achieve spectral selectivity. A common practice is to use narrowband UV filters to block unwanted wavelengths; however, they suffer from lowering of signal intensity, limited band selectivity, and added complexity for integration with CMOS sensors [21]. Recent approaches have focused on methods such as the use of downconverters [12, 22, 23] or the integration of wide bandgap materials in Si-CMOS image sensors [24–33]. Downconverters can enable UV detection by converting UV photons to visible light, but suffer from low conversion efficiency, reduced spatial resolution, broad emission spectra, and low stability. Wide bandgap materials such as ZnO [24], SiC [25], GaN [26, 27], AlGaN [28–31], Ga_2O_3 [32], and thiazolothiazole-based small molecules [33] offer decent UV sensitivity when integrated with CMOS circuitry, but many of these materials are incompatible with standard CMOS processes, respond broadly across the visible and UV spectra, and require dedicated cleanroom fabrication facility which increase cost and complexity. For example, $Al_xGa_{1-x}N$-based solar-blind UV focal plane arrays (FPA) are typically realized by hybrid integration of an AlGaN detector array with a CMOS readout integrated circuit [28–31]. However, this configuration requires complex back-end integration schemes and is constrained by the limited thermal budget of CMOS processing, making monolithic integration and large-scale fabrication challenging. It is important to note that direct monolithic integration of wide-bandgap semiconductor layers with CMOS circuitry via front-end-of-line (FEOL) processes is complex [25, 26]. In contrast, back-end-of-line (BEOL) integration enables low-temperature, post-fabrication processing that preserves CMOS circuitry and allows flexible material deposition, making it widely adopted to extend the range of CMOS image sensors. Due to these drawbacks, existing CMOS-based UV imagers have thus far fallen short of providing true band-selective detection within a single platform. This gap highlights the urgent need for compact, robust, low-cost, and fully CMOS-compatible solutions for high-performance multispectral UV imaging. Moreover, since spectral requirements are strongly use-case dependent, a technology that is easily customizable to specific applications by postprocessing is preferred.

Here we introduce a versatile approach for multispectral UV detection and band-selective UV imaging using CMOS pixelated capacitive sensor (PCS) arrays [34–39]. PCS technology has previously been used for cellular signal detection, microparticle sensing, and oil-water microinterfacial characterization in the 1–100 MHz range [34–39]. We demonstrate that UV sensitivity is achieved by depositing wide-bandgap metal-oxide (MOX) nanoparticle (NP) dispersions onto capacitive sensor pixels, enabling selective detection of UV-A, UV-B, and UV-C bands on a single prefabricated CMOS chip. The MOX-functionalized sensors exhibit readily detectable capacitance increments even under low-intensity UV illumination (0.5 μW cm^{-2}). We employ solution-processed inkjet printing and spin coating techniques to produce multispectral UV detectors and uniform imagers and thereby eliminate the need for high-temperature, sophisticated material-deposition and postprocessing steps. The devices exhibit low noise-equivalent power (NEP, 17–138 fW $Hz^{-1/2}$, Table T1) across the UV bands, and unlike conventional silicon CMOS imagers, our capacitive-CMOS platform is inherently visible-blind. While conventional integration of additional functional layers requires multiple cleanroom steps, increasing complexity and processing time, the present approach uses simple solution-based techniques to enable flexible end-user customization. These fabrication strategies highlight the potential of the PCS platform to realize compact, robust, low-cost multispectral UV imagers, bringing their costs to a level where they might be incorporated in smartphones, allowing everyday users to inspect, e.g., surface cleanliness, food molds, fruit quality, banknote authenticity, sunscreen and makeup coverage.

2 | Results and Discussion

2.1 | Capacitive-CMOS UV Image Sensor Operation

To fabricate the multispectral UV detectors, we use PCS arrays (Figure 1). The monolithic 40 nm CMOS chip contains three separate sensing matrices, each comprising 1024 sensor pixels arranged in a 32 × 32 layout on a pseudo-hexagonal grid (Figure 1a,b, Figures S1 and S2). Matrices 1 and 2 feature square electrodes with dimensions 5 × 5 $μm^2$ and nearest-neighbor pitches of 15 and 10 μm, respectively, while Matrix 3 comprises electrodes with dimensions 4 × 4 $μm^2$ and a 10 μm pitch (Figure S2). Figure 1b demonstrates an isometric view optical micrograph of a selected region of Matrix 1, exhibiting a 3D-like perspective of the pillar-shaped electrodes which form the PCS array and the trenches between the electrodes separating them. The pillar-shaped electrodes are designed to increase the available volume of functional materials for depositing inside trenches, which have a depth of ∼2.25 μm (Figure S3). To validate the construction of a single electrode, we obtained a cross-sectional scanning electron microscopy image of the electrode via targeted focused ion beam milling (Figure 1c). The electrode structure comprises an aluminum core that acts as the conductive electrode, over which first SiO_2 (∼330 nm) and thereafter Si_3N_4 (∼365 nm) layers are deposited. These dielectric layers serve dual purposes: chemical protection against corrosive environments and electrical insulation control to define the effective sensing capacitance. The sense electrodes are aligned directly above the CMOS switching transistor pairs, which are linked through ultra-short vertical stacks made from minimal-area intermediate metal islands and vias to minimize parasitic capacitances. A pair of NMOS/PMOS transistor switches is used to connect each electrode (Figure 1d) to a square wave modulation signal, and to connect surrounding electrodes to ground. The average charging current per modulation signal cycle is measured and translated into an equivalent electrode capacitance. A comprehensive explanation of the PCS chip's working principle is provided in Note S1 (Figures S4–S6).

To fabricate multispectral UV detectors, we deposit high bandgap semiconducting MOX NPs inside the trenches (see later sections). Figure 1d shows a part of the PCS array that is functionalized by MOX NPs. The NPs fill the interpillar trenches, creating an optically active layer inside the sensing region. Illumination by UV light excites free charge carriers in the MOX NPs (Figure 1e), increasing their conductivity. These carriers alter electric fields in the functionalization layer, and consequently modulate the capacitance between the sensing electrodes. This change in capacitance under light exposure in semiconductors, commonly

21983844, 0, Downloaded from https://advanced.onlinelibrary.wiley.com/doi/10.1002/advs.76880 by Joke Dales - Technical University Delft , Wiley Online Library on [03/08/2026]. See the Terms and Conditions (https://onlinelibrary.wiley.com/terms-and-conditions) on Wiley Online Library for rules of use; OA articles are governed by the applicable Creative Commons License

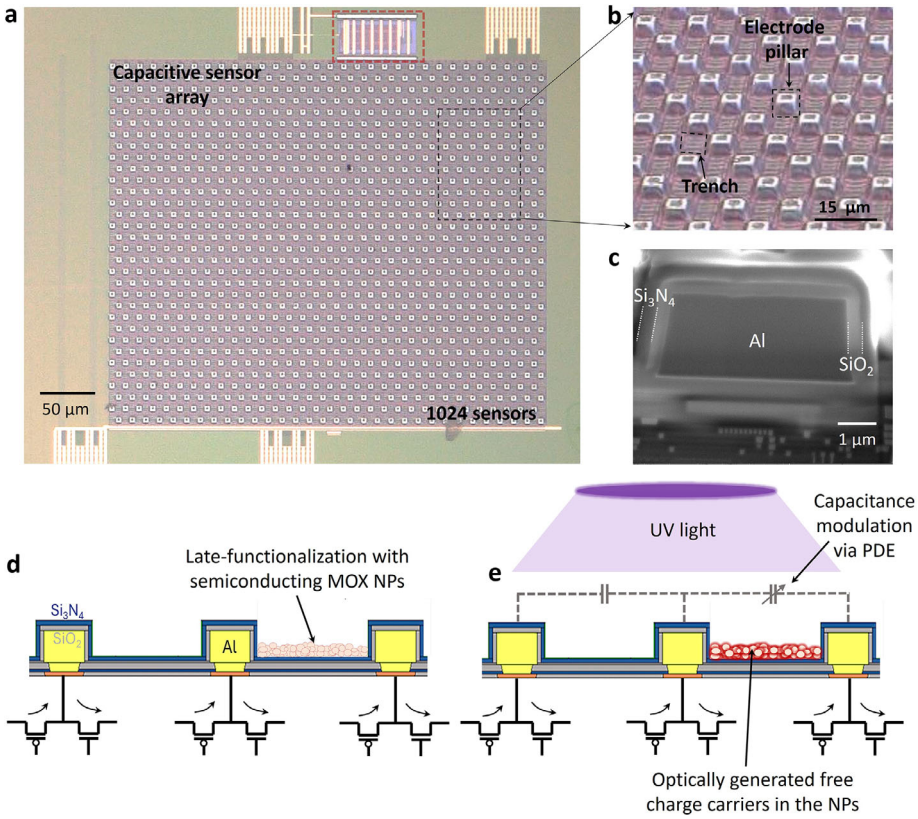


FIGURE 1 | Overview of the capacitive sensor array and its operation principle. (a) Optical microscopy image of the CMOS pixelated capacitive sensor (PCS) chip showing Matrix 1, which contains 1024 individually addressable pixels. The regions of the read-out circuit (consisting of P- and N-current mirrors) are marked with red dashed rectangles. (b) Isometric view of the sensor array under an optical microscope. The structures of pillar-like electrodes and trenches between the electrodes are indicated inside. (c) Cross-sectional scanning electron microscopy image of an electrode-pillar after targeted focused ion beam milling. The electrode consists of an Al metal island, covered by a passivation layer stack of SiO_2 and Si_3N_4. (d) Cross-sectional schematic of the individual sensor pixels. To measure an electrode's capacitance, on-chip PMOS/NMOS switch transistors are used to connect it to a square wave modulation signal and to connect the surrounding electrodes to the ground. The average charging current per modulation signal cycle is measured and, with known modulation voltage amplitude, translated into an equivalent electrode capacitance. A section of the prefabricated chip can be functionalized with high-bandgap semiconducting metal-oxide nanoparticles (MOX NPs). (e) Exposure to UV light with a photon energy exceeding the bandgap of the MOX NPs generates free charge carriers that change the dielectric properties of the NPs and, consequently, the electrode capacitance via the photodielectric effect (PDE).

referred to as the photodielectric effect (PDE), was first reported by Lenard and Saeland [40] and has been observed in various materials [41–44]. PDE can arise from either the excitation of electrons or holes across the bandgap, or the excitation of charges trapped in the bandgap [41–44]. Alternatively, in strongly light-absorbing semiconductors, the Maxwell-Wagner effect [45] can dominate, where light-induced conductivity near the material surface reduces the effective insulating thickness, thereby increasing the capacitance. In MOX NPs, the PDE can originate from both trap-mediated charge polarization and photo-induced conductivity changes, and these contributions can coexist and are often difficult to distinguish experimentally. Here, we leverage the PDE in the NP filled dielectric functionalization layer to convert a CMOS capacitive sensor array into a UV image sensor.

2.2 | Multispectral UV Detection by Nanoparticle Functionalization

To functionalize the capacitive CMOS sensor for UV detection, we prepared aqueous dispersions of semiconducting MOX NPs—ZnO, SnO_2, and Ga_2O_3; chosen for their bandgap energies spanning the UV spectrum (Figure S7). This selection allowed the platform to cover the full range of UV-A, UV-B, and UV-C wavelengths (Figure 2a). To characterize the intrinsic behavior of each material, we first fabricated dedicated chips coated exclusively with one oxide, ensuring that responsivity and noise could be assessed without cross-material interference (Figures S8–S10). For direct comparison, we also drop-coated each dispersion onto separate regions of the same PCS array (Note S1 and Figure S11). The photodetection measurements reveal the spectral selectivity of the MOX films: ZnO exhibited broad UV sensitivity with a peak response under UV-A, SnO_2 responded mainly to wavelengths below UV-B, and Ga_2O_3 was active exclusively under UV-C (Figure 2b, Figure S12). Notably, all devices remained insensitive to visible light (Figure S12a,b).

With these spectral windows established, we quantified the dependence of sensor output on incident UV intensity; a critical parameter for accurate dosimetry and imaging. ZnO, SnO_2, and Ga_2O_3 chips were illuminated with UV-A, UV-B, and UV-C, respectively, at intensities from 0.5 to 500 µW cm^{-2}, and the

21983844, 0, Downloaded from https://advanced.onlinelibrary.wiley.com/doi/10.1002/advs.76880 by Joke Dales - Technical University Delft , Wiley Online Library on [03/08/2026]. See the Terms and Conditions (https://onlinelibrary.wiley.com/terms-and-conditions) on Wiley Online Library for rules of use; OA articles are governed by the applicable Creative Commons License

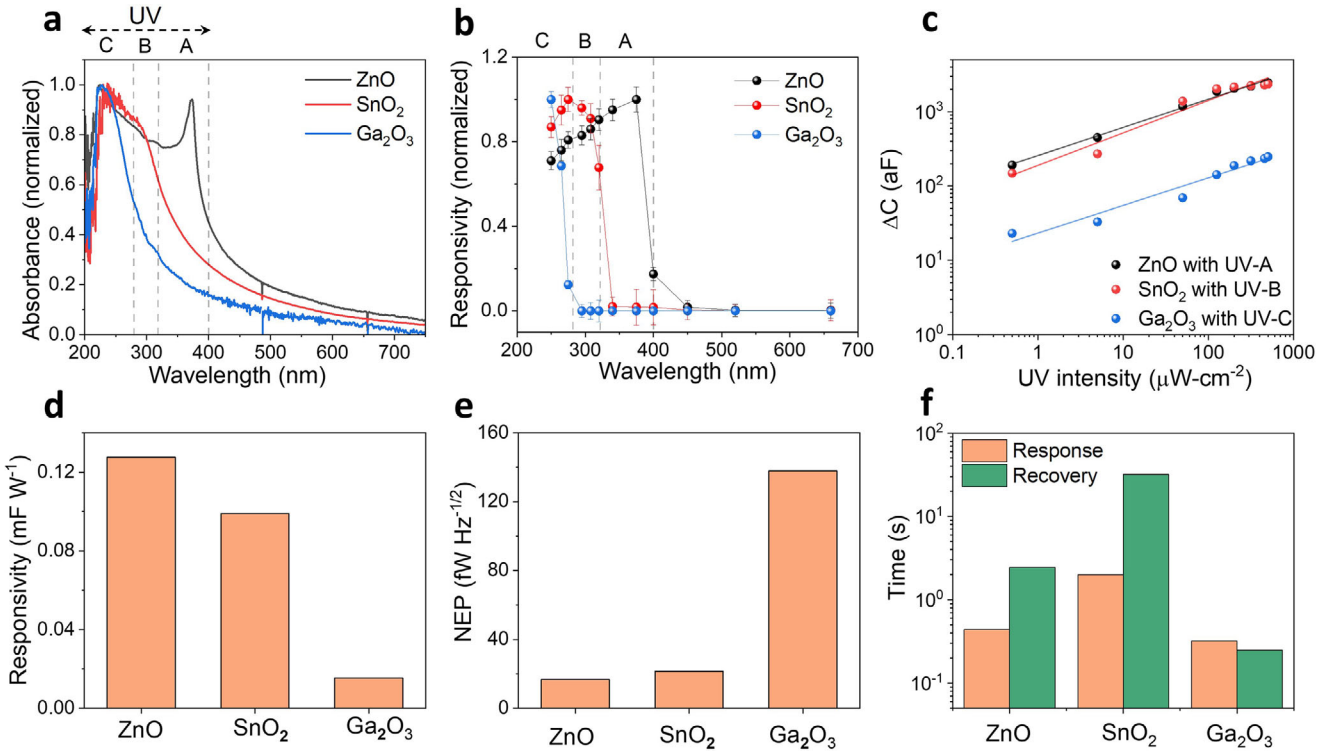


FIGURE 2 | Evaluation of UV-detection performance of the capacitive sensor arrays. (a) Normalized absorbance spectra of ZnO, SnO_2, and Ga_2O_3 NP dispersions in water. (b) Normalized responsivity of the NPs at different exposure wavelengths. Regions corresponding to different UV bands (A, B, and C) are indicated by dashed lines in both a and (b,c). Capacitance changes in ZnO, SnO_2, and Ga_2O_3 NPs under varying UV-A, -B, and -C intensities, respectively. (d) Optimal values of responsivity and (e) noise-equivalent power (NEP) achieved with the ZnO, SnO_2 and Ga_2O_3 NPs under UV light (A, B, C, respectively). (f) Response and recovery times of the ZnO, SnO_2 and Ga_2O_3 NP-coated pixels. ZnO and SnO_2 chips were cured at 100°C and 200°C, respectively, for 10 min. Ga_2O_3 chip was cured at room-temperature.

most responsive pixels were identified (Figure 2c). ZnO and SnO_2 exhibited capacitance increases up to 13× (191 to 2462 aF) and 16× (149 to 2362 aF), respectively, while Ga_2O_3 increased ~11× under UV-C (23 to 248 aF); however, the absolute magnitudes were roughly one order lower than those of ZnO and SnO_2 (Figure 2c). These observed increments surpass the system's minimum quantifiable capacitance (3.3 aF) by ~7-746×, thereby ensuring reliable detection of low-intensity UV signals in the present CMOS sensor. We also observed that Matrix 1 consistently produced the strongest signals (Figure S13) due to its larger channel volume and was thus selected for all subsequent analyses.

From these optimized pixels, we determined maximum responsivities of 0.13, 0.10, and 0.015 mF W^{-1} for ZnO, SnO_2, and Ga_2O_3, respectively (Figure 2d, Figures S14 and S15). It is important to note that the responsivity unit in capacitive sensors (F W^{-1}) is different from that used for conventional charge-based photodetectors (A W^{-1}; Table T1), and, therefore, it is better to compare sensor performance by their noise-equivalent power (NEP). The corresponding NEP values were 17, 22, and 138 fW $Hz^{-1/2}$ (Figure 2e, Figure S16), comparable to those of state-of-the-art UV detectors that typically range from a few to several thousand fW $Hz^{-1/2}$ (Table T1). Finally, we evaluated the temporal response to assess suitability for real-time imaging. Ga_2O_3 pixels exhibited fast and highly repeatable dynamics, with response and recovery times of 0.32 and 0.25 s, respectively (Figure 2f, Figure S17), limited primarily by the microcontroller sampling rate. Room-temperature-cured ZnO and SnO_2 films were slower (Figures S18a and S19a) due to trap-mediated charge dynamics; that were subsequently improved by thermal curing. ZnO pixels cured at 100°C demonstrated markedly improved dynamics owing to defect-state removal [46], with response and recovery times of 0.44 and 2.45 s, respectively; 1–2 orders of magnitude faster than the as-deposited device (Figure S18). SnO_2 required 200°C curing to achieve faster response (~18 s, Figure S19c), although residual deep-trap effects remained, likely due to defects in the NPs and might be improved with further research [47]. To further improve, SnO_2 powder was thermally cured in an oven at 300°C and 500°C for 2 h in ambient air, after which the nanoparticles were deposited onto the sensor pixels. We observed significantly improved device performance under these conditions. For 300°C-cured SnO_2 nanoparticles, the response and recovery times were 2 and 31.8 s, respectively (Figure S19d). For 500°C-cured SnO_2 nanoparticles, the response and recovery times further improved to 1.5 and 8.7 s, respectively (Figure S19e).

To understand how the effective relative permittivity (ε_{eff}) of the deposited MOX NPs influences the capacitance of the sensor pixels, we performed finite-element simulations using COMSOL Multiphysics (Note S3 and Figure S20). The simulated trends aligned well with the results shown in Figure 2c. These insights allow the capacitance change to be expressed as $\Delta C \propto \varepsilon_{eff}(I)$, where ε_{eff} varies with UV intensity (I).

21983844, 0, Downloaded from https://advanced.onlinelibrary.wiley.com/doi/10.1002/advs.76880 by Joke Dales - Technical University Delft , Wiley Online Library on [03/08/2026]. See the Terms and Conditions (https://onlinelibrary.wiley.com/terms-and-conditions) on Wiley Online Library for rules of use; OA articles are governed by the applicable Creative Commons License

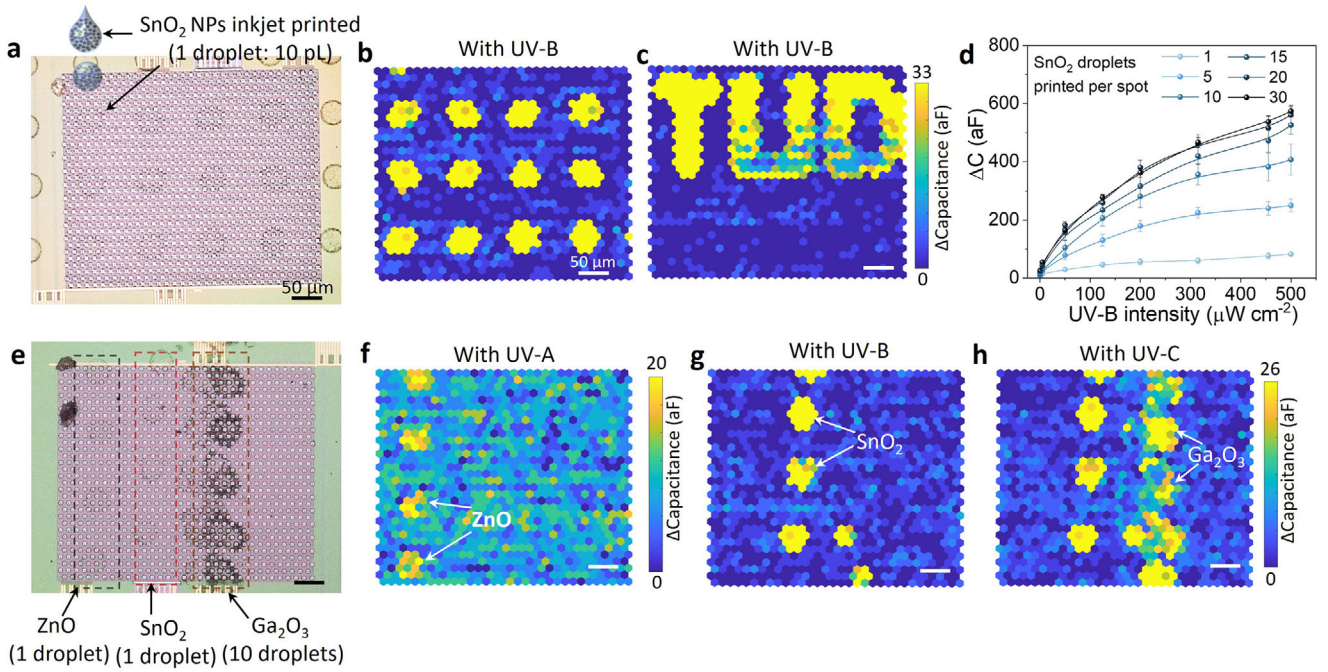


FIGURE 3 | Capacitive CMOS sensor functionalized by inkjet printing. (a) Optical microscopy image of Matrix 1 inkjet-coated with SnO_2 NP droplets (1 droplet with a volume of 10 pL) in a controlled grid. A schematic representation of inkjet droplets is shown above the figure. (b) Response of Matrix 1 exposed under UV-B. Only SnO_2-functionalized pixels show response under UV-B. (c) Response with UV-B, where the letters "TUD" were inkjet printed on Matrix 1 using the SnO_2 ink droplets. (d) Capacitance variation of the sensor pixels inkjet-coated with different numbers of SnO_2 ink droplets (1–30) per spot under varying UV-B intensities (0.5–500 µW cm^{-2}). (e) Optical microscopy image of Matrix 1 inkjet-coated with 10 pL droplets of ZnO (1 droplet per spot), SnO_2 (1 droplet per spot) and Ga_2O_3 (10 droplets per spot), facilitating multispectral UV detection within a single array. Response of Matrix 1 with (f) UV-A, (g) UV-B, and (h) UV-C, respectively. The scale bars in c, e, f, g, and h represent 50 µm. The capacitance scale bar for b and c is shown to the right of c, and for g and h, to the right of h.

Collectively, these results confirm the origin of the observed UV-response from the PDE, which is strongly correlated with the bandgap of the sensing material. Moreover, insights from these drop-cast experiments motivated us to explore more precise and scalable functionalization strategies to enable UV imaging with the capacitive CMOS arrays.

2.3 | Multispectral Imaging With Inkjet-Printed Sensors

Multispectral imaging on CMOS platforms requires precise, scalable functionalization of individual pixels with wavelength-selective materials, which cannot be reliably achieved through drop casting. To meet this requirement, we adopted inkjet printing as an alternate strategy for spatially selective deposition (Figure 3). Beyond its sustainability and material efficiency, inkjet printing enables precise placement of picolitre-scale droplets [48], offering a route to integrate ultralow quantities of functional materials directly onto CMOS pixels. Although inkjet patterning of CMOS substrates has been demonstrated for humidity sensing using graphene and metal-oxide systems [49, 50], its potential for CMOS-integrated photodetection has remained largely unexamined.

We therefore sought to exploit the synergy between the localization afforded by inkjet deposition and the intrinsic versatility of PCS-based photodetection. By doing so, we aimed to establish a generalizable method for creating highly resolved, on-chip patterns of UV-responsive materials that could enable multispectral imaging. To this end, we formulated a suite of inkjet-printable MOX inks (Figures S21–S23) and used them to deposit 10 pL SnO_2 droplets in a controlled grid on Matrix 1 (Figure 3a). This configuration allowed us to evaluate both the spatial precision of the printing process and the photodetection capabilities of individual, selectively coated pixels. Each droplet reliably covered 14–15 pixels, and an array of 16 droplets with ~100 µm spacing provided a well-defined testbed.

Under UV-B illumination (250 µW cm^{-2}), pixels coated with SnO_2 exhibited clear capacitive responses reaching 49.7 ± 7.5 aF (Figure 3b, Figure S24 and Table T2). These measurements confirm that even picolitre-scale depositions, nearly five orders of magnitude smaller than conventional drop-cast volumes, contain sufficient NP loading to activate UV responsiveness. The positional accuracy of inkjet printing further enabled deliberate patterning: printing the letters "TUD" (Figure S25) produced a latent image that became visible only under UV-B excitation (Figure 3c), illustrating the capacity to encode and reveal information on demand.

To understand the relationship between droplet morphology and device response, we examined the NP distribution within the printed droplets. SEM imaging revealed peripheral densification consistent with the coffee-ring effect (Figures S26–S31), which reduces uniformity when only a single droplet is deposited. By

21983844, 0, Downloaded from https://advanced.onlinelibrary.wiley.com/doi/10.1002/advs.76880 by Jake Dates - Technical University Delft , Wiley Online Library on [03/08/2026]. See the Terms and Conditions (https://onlinelibrary.wiley.com/terms-and-conditions) on Wiley Online Library for rules of use; OA articles are governed by the applicable Creative Commons License

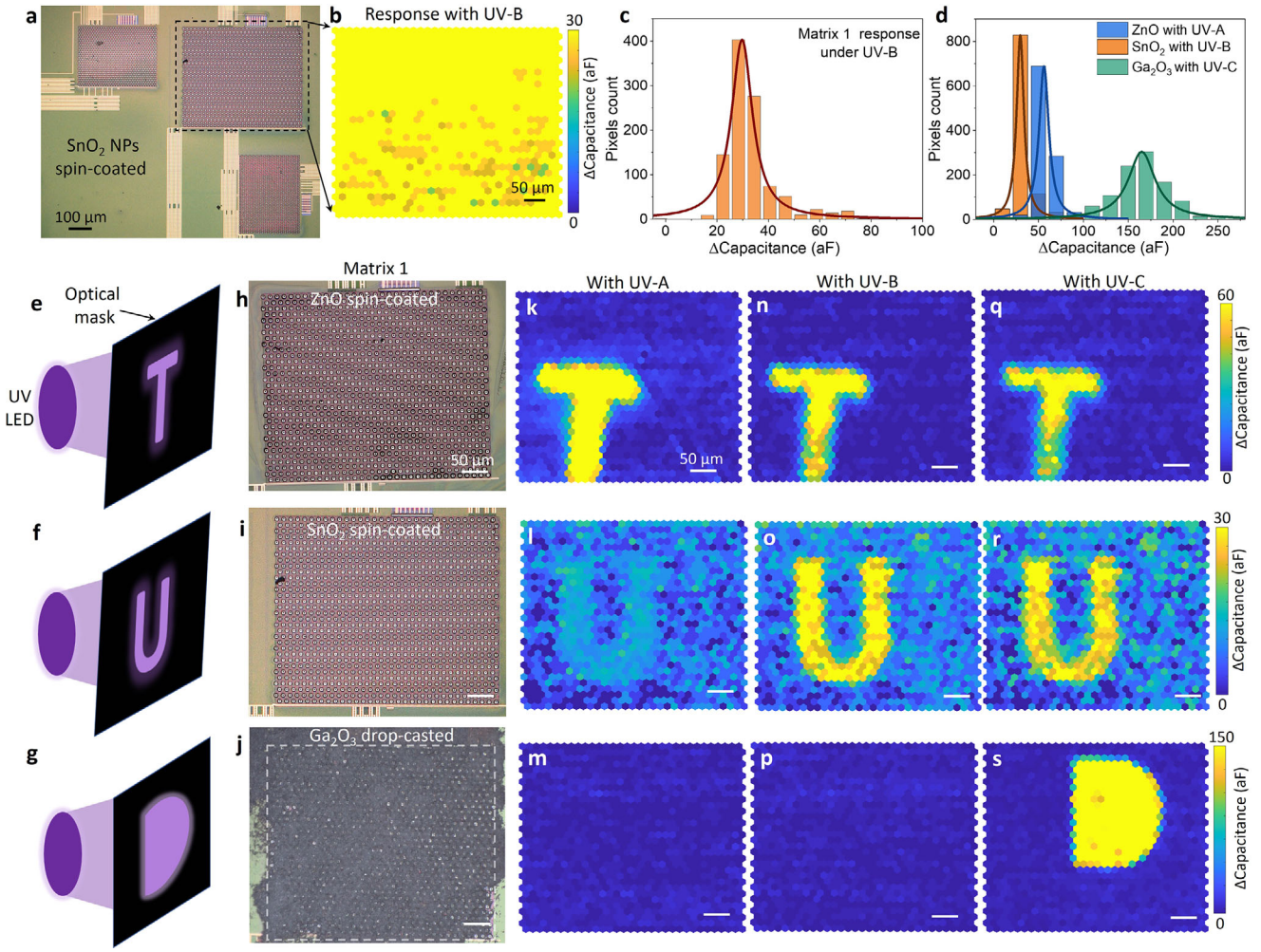


FIGURE 4 | Capacitive CMOS sensor functionalized by spin coating. (a) Optical microscopy image of SnO_2-NPs spin-coated on PCS arrays. (b) Capacitive response of SnO_2-coated Matrix 1 under UV-B exposure (0.25 mW cm^{-2}), indicating uniform responses from the majority of the pixels. (c) The distribution of capacitive responses in Matrix 1 of the SnO_2 spin-coated chip under UV-B light. (d) The distribution of pixel responses for ZnO, SnO_2 spin-coated and Ga_2O_3 drop-casted chips under UV-A, UV-B and UV-C illumination, respectively, at similar intensities (0.25 mW cm^{-2}). (e–g) Schematics of the optical shadow masks of the letters "T", "U" and "D" for UV light to pass through and projected on Matrix 1 of (h) ZnO, (i) SnO_2 spin-coated and (j) Ga_2O_3 drop-coated chips. The response of ZnO, SnO_2 and Ga_2O_3-coated pixels under (k–m) UV-A, (n–p) UV-B, and (q–s) UV-C, respectively. Scale bars in i, j, l-s represent 50 µm. The capacitance scale bar for k, n and q is shown to the right of q; for l, o and r is shown to the right of r; and for m, p and s is shown to the right of s.

printing multiple droplets at the same location, we increased the NP density and improved the coverage uniformity, resulting in progressively larger photoresponses. For SnO_2, increasing the droplet count from 1 to 30 enhanced the UV-B-induced (500 µW cm^{-2}) capacitance change from 82 to 573 aF (Figure 3d, Figure S26). This tunability demonstrates that inkjet printing not only offers spatial selectivity but also provides a means of controlling responsivity via local material loading.

Comparative experiments with ZnO and Ga_2O_3 inks highlight the generality of the approach while revealing material-specific performance limits. ZnO produced lower UV-A responses (13–71 aF, Figure S32a), aligned with its reduced NP concentration (Figures S27–S30), whereas Ga_2O_3 droplets generated the smallest changes under UV-C (14–27 aF, Figure S32b). Responsivity and NEP values followed the same trend (Figure S33) and, as expected, remained 2–3 orders of magnitude lower than those of drop-cast films due to the much lower NP loadings.

Building on these insights, we extended our approach to achieve multispectral UV detection within a single array. We deposited 10 pL droplets of ZnO (1 droplet), SnO_2 (1 droplet), and Ga_2O_3 (10 droplets) at predefined locations on Matrix 1 (Figure 3e), creating spatially isolated pixels with distinct spectral sensitivities. A greater number of Ga_2O_3 droplets was required to achieve measurable response due to its intrinsically lower UV-C responsivity. This heterogeneous functionalization enabled selective detection of UV-A, UV-B, and UV-C illumination across the same device (Figure 3f–h).

Further, the fabricated devices also exhibited low drift (Figure S34), repeatable response (Figure S35), high reproducibility (Figure S36), and long-term stability (Figure S37). Together, these results validate inkjet printing as a practical and highly controllable route to spatially selective functionalization of CMOS imagers, providing the foundation for scalable multispectral UV

21983844, 0, Downloaded from https://advanced.onlinelibrary.wiley.com/doi/10.1002/advs.76880 by Jake Dales - Technical University Delft , Wiley Online Library on [03/08/2026]. See the Terms and Conditions (https://onlinelibrary.wiley.com/terms-and-conditions) on Wiley Online Library for rules of use; OA articles are governed by the applicable Creative Commons License

sensing and enabling new modalities such as on-chip optical encoding.

2.4 | Imaging With Spin-Coated Sensors

Finally, we investigated the imaging capabilities of uniformly coated PCS arrays. Uniformity in pixel response is essential for accurate UV imaging, as variations in the sensing layer can directly translate into spatial artifacts in the reconstructed images. To ensure consistent pixel behavior, we implemented an easily applicable spin-coating approach to deposit MOX NP films across the PCS arrays (Figure 4). This method produced highly uniform SnO_2 coatings (Figure 4a, Figure S38), which in turn enabled consistent UV-B responses across all three matrices (Figure 4b, Figure S39). Matrix 1, benefiting from its wider channels, facilitates more even NP spreading and delivers the highest uniformity, with pixel responses clustered tightly around 33 ± 5 aF (Figure 4c,d). A similarly uniform response was obtained using spin-coated ZnO films, with UV-A sensitivity reaching 58 ± 10 aF (Figure 4d). Ga_2O_3, which exhibits intrinsically weaker capacitive response magnitude under UV-C (Figure 2d, Figures S12–S14) due to lower photocarrier generation efficiency while compared to ZnO and SnO_2, was not compatible with spin coating as it required a thicker film to generate measurable signals. For this reason, we employed drop-casting to achieve higher material loading as increasing the amount of photoactive material promotes greater UV absorption, carrier generation, resulting in a higher capacitance change (Figure S10). While this approach yielded sufficient sensitivity under UV-C illumination, the resulting films were less homogeneous, leading to a broader response distribution (162 ± 32 aF, Figure 4d).

With these optimized sensing layers, we next evaluated the ability of the PCS arrays to resolve spatial UV patterns (Figure 4e–s). Each film was illuminated through a laser-milled metallic shadow mask containing the letters “T”, “U”, and “D” (Figure S40). This enables direct assessment of spectral selectivity and imaging fidelity. ZnO, which is responsive across a broad UV spectrum, clearly resolved the letter “T”, most prominently under UV-A. SnO_2, which is selectively sensitive to UV-B, produced a strong and well-defined “U”, while Ga_2O_3 responded exclusively under UV-C, enabling sharp visualization of the letter “D”. The slightly enlarged appearance of the reconstructed features is likely due to variations in the angles of incidence of the light beams that pass through the metal masks.

Furthermore, to probe the dynamic performance, we tracked a moving UV source across the chip surface (Note S4, Figures S41 and S42). The device successfully captured temporal shifts in illumination, endorsing the capability of the PCS platform for real-time UV imaging, in which the sensing modality can be tuned simply by selecting the appropriate oxide film.

3 | Conclusion

Here, we developed capacitive CMOS sensors for multispectral UV imaging that contain 32 × 32 pixels each in three individually addressable arrays, and allow use-case-specific late-functionalization of the chip surface outside the foundry. To activate the sensors for selectively detecting different UV bands, we utilized wide-bandgap semiconducting MOX NPs. Unlike conventional charge-based imagers, the present device employs a capacitive operation principle where UV light causes capacitance changes in the functionalization layer via PDE. Under UV exposure (500 μW cm^{-2}), MOX-functionalized pixels produce high capacitance variations (up to 2462 aF), which can be readily detected, as these responses are nearly 746× the lowest quantifiable capacitance-response. Across UV bands, the sensors exhibit low NEP (17-138 fW $Hz^{-1/2}$), comparable to state-of-the-art UV detectors, which typically range from a few to several thousand fW $Hz^{-1/2}$. Furthermore, the use of precision inkjet printing enables highly localized functionalization and supports multispectral UV detection within a single array, demonstrating the versatility of the capacitive-CMOS platform even with ultralow material volumes (10 pL). However, in the current inkjet-printed array, each droplet spreads over multiple pixels (~14-15), limiting the effective spatial resolution. This spreading arises from the wetting behavior of the nanoparticle solution, influenced by the surface energy of the substrate, solvent properties, and nanoparticle concentration. Pixel-level functionalization could be achieved in the future via reduced droplet volumes, surface treatments, optimized ink rheology, or alternative patterning techniques. Additionally, spin-coating of functional MOX layers enables uniform, high-resolution, and band-selective UV imaging without relying on intricate high-temperature processes typically required for standard CMOS imagers. It should be noted that the electrical response of the MOX layers is known to be influenced by environmental factors such as temperature, humidity, and oxygen adsorption. Future work will therefore focus on systematically investigating device behavior under varying environmental conditions and developing mitigation strategies to improve environmental stability. This work, thus, establishes a scalable, sustainable, and fully CMOS-compatible strategy for fabricating low-cost multispectral UV imagers with the potential for extension to other spectral regions. Beyond imaging, the present work also opens new avenues for developing versatile, monolithic multisensing platforms, where integrating diverse functional materials could enable detection of a wide range of external stimuli, paving the way for future applications.

4 | Experimental Section

4.1 | Deposition of Metal-Oxide Nanoparticle Dispersions

Dispersions (5 wt.%) of ZnO, SnO_2 (~100 nm), and Ga_2O_3 nanoparticles (Sigma-Aldrich) were prepared in deionized water and ultrasonicated for 2 h. The dispersions of volume ~1 μL were drop-cast onto the chips. To deposit 3 different types of MOX NPs onto a single chip, we used syringes mounted on a Hyrel printer equipped with a micropositioner and optical camera, which allows accurate dispensing (~1 μL) onto defined regions of the PCS arrays.

4.2 | Spin Coating of Metal-Oxide Nanoparticle Inks

ZnO (in isopropyl alcohol) and SnO_2 (in butanol) inks (particle size <20 nm, Sigma–Aldrich) were used without modification. Uniform films were formed by spin-coating 1 μL of the ink at

21983844, 0, Downloaded from https://advanced.onlinelibrary.wiley.com/doi/10.1002/advs.76880 by Joke Dales - Technical University Delft , Wiley Online Library on [03/08/2026]. See the Terms and Conditions (https://onlinelibrary.wiley.com/terms-and-conditions) on Wiley Online Library for rules of use; OA articles are governed by the applicable Creative Commons License

1500 rpm for 1 min, followed by room-temperature drying for 1 h. The thickness of the ZnO-NPs spin-coated film was 337 ± 17 nm, and for SnO_2 film, the thickness was 148 ± 4 nm.

4.3 | Inkjet Printing of Metal-Oxide Nanoparticle Inks

Inkjet printable ink solutions were prepared by dispersing ZnO, SnO_2, and Ga_2O_3 NPs (5 wt.%) in a 1:9 ethanol-water mixture. To lower the surface tension of the ink, sodium dodecyl sulfate (0.2 wt.%) was added as a surfactant. The mixture was then ultrasonicated for 4 h and subsequently stirred for 4 days to yield stable NP ink solutions. Dynamic light scattering (DLS) confirmed the presence of well-dispersed ZnO, SnO_2, and Ga_2O_3 nanoparticles with average hydrodynamic particle diameters of 314, 338, and 325 nm, respectively (Figure S21), which are well below the 22 µm nozzle-width of the inkjet printer, minimizing the risk of clogging[48]. The viscosity (1.05-1.1 mPa s, Figure S22) and surface tension (33–38 mN m^{-1}, Figure S22) of the prepared inks also fall within the printable range[48], enabling the formation of stable, well-defined and repeatable inkjet droplets (Figure S23). Inkjet printing was performed using a PiXDRO LP50 inkjet printer with DMC-11610 cartridges, which produced 10 pL droplets.

4.4 | Photodetection Measurements

Photodetection was carried out using LEDs (Thorlabs) with defined peak wavelengths. For the experiments (except Figure 2b), we employed LEDs with defined peak emission wavelengths of 375 nm (LED375L, Thorlabs, bandwidth (FWHM) ≈ 10 nm), 310 nm (LED310W, Thorlabs, bandwidth (FWHM) ≈ 15 nm), and 255 nm (LED255J, Thorlabs, bandwidth (FWHM) ≈ 12 nm) to represent UV-A, UV-B, and UV-C radiation, respectively. LED intensities were tuned with a neutral density filter (NDC-50S-3 M, Thorlabs) and calibrated using a Thorlabs PM100A power meter coupled to an S401C sensor. The PCS arrays were then exposed to the LEDs, and capacitance values were recorded with a measurement board (Figure S6). All measurements were conducted under stable ambient conditions (25°C ± 2°C, 55% ± 3% RH). Prior to the experiments, packaged PCS chips (received from NXP Semiconductors) were cleaned with deionized water and isopropyl alcohol.

4.5 | Calculation of Responsivity and Noise-Equivalent Power (NEP)

The responsivity (R) in F W^{-1} was calculated using the following formula:

$$R = \frac{\Delta C}{P \times A}$$

where ΔC is the capacitance change under UV exposure with respect to the capacitance under dark conditions, P is the intensity of the incident light, and A is the active area under illumination ≈ 300 μm^2 (see Figure S16).

The NEP in W $Hz^{-1/2}$ was calculated using the following formula:

$$NEP = \sigma_{noise} \times \sqrt{\frac{2}{f_{sampling}}} \times \frac{1}{R}$$

where, $f_{sampling}$ is the sampling rate = 4.55 Hz, σ_{noise} is the standard deviation of measured noise = 3.21 aF (Figure S16).

Author Contributions

Murali K. Ghatkesar, Peter G. Steeneken and Frans P. Widdershoven contributed equally to this work. **Suman Kundu**: conceptualization, methodology, software, data curation, formal analysis, validation, investigation, visualization, Writing – original draft, Writing – review and editing. **Kai Betlem**: data curation, validation, visualization, writing – original draft, writing – review and editing, formal analysis. **Tao Shen**: software, data curation, validation, visualization, writing – original draft, writing – review and editing, formal analysis.

Acknowledgements

Authors acknowledge the facilities of the Department of Microelectronics (Bioelectronics Section) and the Department of Precision and Microsystems Engineering, TU Delft. The authors acknowledge the funding by the European Union's Horizon Europe Coordination and Support Programme, Grant Agreement No: 101136388. S.K. and F.P. W. acknowledge funding from the European Union Horizon 2020 programme for project Distributed Artificial Intelligent System (DAIS), Grant agreement number: 101007273. P.G.S. and M.K.G. acknowledge support from the Dutch government as part of the National Growth Fund programme NXTGEN Hightech, project Agrifood 11: Greenhouse Horticulture—Digital Twin. P.G.S. acknowledges funding from the European Union under the Horizon Europe Programme, Grant Agreement No. 101136388 (Team Nano).

Conflicts of Interest

The Authors declare no conflicts of interest.

Data Availability Statement

The data that support the findings of this study are available from the corresponding authors upon reasonable request.

References

1. A. El Gamal and H. Eltoukhy, "CMOS Image Sensors," *IEEE Circuits and Devices Magazine* 21, no. 3 (2005): 6–20, https://doi.org/10.1109/MCD.2005.1438751.

2. M. Bigas, E. Cabruja, J. Forest, and J. Salvi, "Review of CMOS Image Sensors," *Microelectronics journal* 37, no. 5 (2006): 433–451, https://doi.org/10.1016/j.mejo.2005.07.002.

3. A. J. P. Theuwissen, "CMOS Image Sensors: State-of-the-art," *Solid-State Electronics* 52, no. 9 (2008): 1401–1406, https://doi.org/10.1016/j.sse.2008.04.012.

4. M. Zhang and A. Bermak, "CMOS Image Sensor With on-Chip Image Compression: A Review and Performance Analysis," *Journal of Sensors* 2010, no. 1 (2010): 920693, https://doi.org/10.1155/2010/920693.

5. S. Goossens, G. Navickaite, C. Monasterio, et al., "Broadband image sensor array based on graphene–CMOS integration," *Nature Photonics* 11, no. 6 (2017): 366–371, https://doi.org/10.1038/nphoton.2017.75.

6. M. Yako, Y. Yamaoka, T. Kiyohara, et al., "Video-rate hyperspectral camera based on a CMOS-compatible random array of Fabry–Pérot

21983844, 0, Downloaded from https://advanced.onlinelibrary.wiley.com/doi/10.1002/advs.76880 by Jake Dales - Technical University Delft , Wiley Online Library on [03/08/2026]. See the Terms and Conditions (https://onlinelibrary.wiley.com/terms-and-conditions) on Wiley Online Library for rules of use; OA articles are governed by the applicable Creative Commons License

filters," *Nature Photonics* 17, no. 3 (2023): 218–223, https://doi.org/10.1038/s41566-022-01141-5.

7. M. Yang, R. Douglas, C. Li, et al., "Dynamic Range and Precision of Hybrid Vision Sensors," *Nature* 642, no. 8066 (2025): E7–E8, https://doi.org/10.1038/s41586-025-08991-3.

8. J. Shi, D. Yoo, F. Vidal-Codina, et al., "A Room-temperature Polarization-sensitive CMOS Terahertz Camera Based on Quantum-Dot-Enhanced Terahertz-To-Visible Photon Upconversion," *Nature nanotechnology* 17, no. 12 (2022): 1288–1293, https://doi.org/10.1038/s41565-022-01243-9.

9. S. Tsarev, D. Proniakova, X. Liu, et al., "Vertically Stacked Monolithic Perovskite Colour Photodetectors," *Nature* 642, no. 8068 (2025): 592–598, https://doi.org/10.1038/s41586-025-09062-3.

10. Z. Li, T. Yan, and X. Fang, "Low-Dimensional Wide-bandgap Semiconductors for UV Photodetectors," *Nature Reviews Materials* 8, no. 9 (2023): 587–603, https://doi.org/10.1038/s41578-023-00583-9.

11. J. Kim, S.-M. Kwon, Y. K. Kang, et al., "A Skin-Like Two-dimensionally Pixelized Full-color Quantum Dot Photodetector," *Science advances* 5, no. 11 (2019): aax8801, https://doi.org/10.1126/sciadv.aax8801.

12. C. Chen, Z. Wang, J. Wu, et al., "Bioinspired, vertically stacked, and perovskite nanocrystal–enhanced CMOS imaging sensors for resolving UV spectral signatures," *Science Advances* 9, no. 44 (2023): adk3860, https://doi.org/10.1126/sciadv.adk3860.

13. M. Liu, N. Yazdani, M. Yarema, M. Jansen, V. Wood, and E. H. Sargent, "Colloidal Quantum Dot Electronics," *Nature Electronics* 4, no. 8 (2021): 548–558, https://doi.org/10.1038/s41928-021-00632-7.

14. G. Arquer, F. Pelayo, A. Armin, P. Meredith, and E. H. Sargent, "Solution-processed Semiconductors for next-generation Photodetectors," *Nature Reviews Materials* 2, no. 3 (2017): 1–17, https://doi.org/10.1038/natrevmats.2016.100.

15. D. Baierl, L. Pancheri, M. Schmidt, et al., "A Hybrid CMOS-imager With a Solution-processable Polymer as Photoactive Layer," *Nature communications* 3, no. 1 (2012): 1175, https://doi.org/10.1038/ncomms2180.

16. A. Kalra, U. U. Muazzam, R. Muralidharan, S. Raghavan, and D. N. Nath, "The Road Ahead for Ultrawide Bandgap Solar-blind UV Photodetectors," *Journal of Applied Physics* 131, no. 15 (2022): 150901, https://doi.org/10.1063/5.0082348.

17. L. Guo, Y. Guo, J. Wang, and T. Wei, "Ultraviolet Communication Technique and Its Application," *Journal of Semiconductors* 42, no. 8 (2021): 081801, https://doi.org/10.1088/1674-4926/42/8/081801.

18. M. Raeiszadeh and B. Adeli, "A Critical Review on Ultraviolet Disinfection Systems Against COVID-19 Outbreak: Applicability, Validation, and Safety Considerations," *Acs Photonics* 7, no. 11 (2020): 2941–2951, https://doi.org/10.1021/acsphotonics.0c01245.

19. C. Avila-Avendano, M. I. Pintor-Monroy, A. Ortiz-Conde, J. A. Caraveo-Frescas, and M. A. Quevedo-Lopez, "Deep UV Sensors Enabling Solar-blind Flame Detectors for Large-area Applications," *IEEE Sensors Journal* 21, no. 13 (2021): 14815–14821, https://doi.org/10.1109/JSEN.2021.3071980.

20. D. Prutchi, *Exploring Ultraviolet Photography: Bee Vision, Forensic Imaging, and Other Near-Ultraviolet Adventures With Your DSLR* (Amherst Media, 2016).

21. M. B. Lindner, S. Elstein, J. Wallace, and P. Lindner, "Solar Blind Bandpass Filters for UV Imaging devices," in *Digital Solid State Cameras: Designs and Applications* (SPIE, 1998), 176–183, https://doi.org/10.1117/12.304582.

22. A. Saha, G. Kumar, S. Pradhan, G. Dash, R. Viswanatha, and G. Konstantatos, "Visible-Blind ZnMgO Colloidal Quantum Dot Downconverters Expand Silicon CMOS Sensors Spectral Coverage Into Ultraviolet and Enable UV-Band Discrimination," *Advanced Materials* 34, no. 10 (2022): 2109498, https://doi.org/10.1002/adma.202109498.

23. X. Wang, Y. Chen, F. Liu, and Z. Pan, "Solar-blind Ultraviolet-C Persistent Luminescence Phosphors," *Nature Communications* 11, no. 1 (2020): 2040, https://doi.org/10.1038/s41467-020-16015-z.

24. X. Du, Z. Mei, Z. Liu, et al., "Controlled Growth of High-Quality ZnO-Based Films and Fabrication of Visible-Blind and Solar-Blind Ultra-Violet Detectors," *Advanced Materials* 21, no. 45 (2009): 4625–4630, https://doi.org/10.1002/adma.200901108.

25. J. Romijn, S. Vollebregt, L. M. Middelburg, et al., "Integrated 64 Pixel UV Image Sensor and Readout in a Silicon Carbide CMOS Technology," *Microsystems & Nanoengineering* 8, no. 1 (2022): 114, https://doi.org/10.1038/s41378-022-00446-3.

26. C.-J. Lee, C.-H. Won, M. Bae, J.-K. Shin, J.-H. Lee, and S.-H. Hahm, "Hybrid UV Active Pixel Sensor Implemented Using GaN MSM UV Sensor and Si-based Circuit," *IEEE Sensors Journal* 15, no. 9 (2015): 5071–5074, https://doi.org/10.1109/JSEN.2015.2433939.

27. B. Chen, J. Zhu, S. Wei, et al., "High-Performance Zero-Powered InHfO/GaN Photodetectors for Ultraviolet Image Sensing Systems," *ACS Applied Electronic Materials* 7, no. 7 (2025): 2793–2802, https://doi.org/10.1021/acsaelm.4c02279.

28. Q. Cai, H. You, H. Guo, et al., "Progress on AlGaN-based Solar-blind Ultraviolet Photodetectors and Focal Plane Arrays," *Light: Science & Applications* 10, no. 1 (2021): 94, https://doi.org/10.1038/s41377-021-00527-4.

29. P. Lamarre, A. Hairston, S. P. Tobin, et al., "AlGaN UV Focal Plane Arrays," *Physica Status Solidi (a)* 188, no. 1 (2001): 289–292, https://doi.org/10.1002/1521-396X(200111)188:1%3C289::AID-PSSA289%3E3.0.CO;2-U.

30. R. McClintock, A. Yasan, K. Mayes, P. Kung, and M. Razeghi, "Back-illuminated Solar-blind Photodetectors for Imaging Applications," in *Quantum Sensing and Nanophotonic Devices II* (SPIE, 2005), 175–184, https://doi.org/10.1117/12.597077.

31. J.-L. Reverchon, J.-A. Robo, and J.-P. Truffer, "AlGaN-based Focal Plane Arrays for Selective UV Imaging at 310Nm and 280Nm and Route Toward Deep UV Imaging," in *Sensors, Systems, and Next-Generation Satellites XI* (SPIE, 2007), 314–322, https://doi.org/10.1117/12.754794.

32. Y. Qin, L.-H. Li, Z. Yu, et al., "Ultra-high Performance Amorphous Ga_2O_3 Photodetector Arrays for Solar-blind Imaging," *Advanced Science* 8, no. 20 (2021): 2101106, https://doi.org/10.1002/advs.202101106.

33. J. Park, W. J. Pyo, J. Kang, et al., "Rational Molecular Design of π-Extended Thiazolothiazole for High-Performance UV-OPDs Seamlessly Integrated With CMOS," *Advanced Materials* 37, no. 38 (2025): 2506449, https://doi.org/10.1002/adma.202506449.

34. C. Laborde, F. Pittino, H. A. Verhoeven, et al., "Real-time Imaging of Microparticles and Living Cells With CMOS Nanocapacitor Arrays," *Nature Nanotechnology* 10, no. 9 (2015): 791–795.

35. A. Cossettini, C. Laborde, D. Brandalise, F. Widdershoven, S. G. Lemay, and L. Selmi, "Space and Frequency Dependence of Nanocapacitor Array Sensors Response to Microparticles in Electrolyte," *IEEE Sensors Journal* 21, no. 4 (2020): 4696–4704, https://doi.org/10.1109/JSEN.2020.3032712.

36. S. G. Lemay, C. Laborde, C. Renault, A. Cossettini, L. Selmi, and F. P. Widdershoven, "High-frequency Nanocapacitor Arrays: Concept, Recent Developments, and Outlook," *Accounts of Chemical Research* 49, no. 10 (2016): 2355–2362, https://doi.org/10.1021/acs.accounts.6b00349.

37. F. Widdershoven, A. Cossettini, C. Laborde, et al., "A CMOS Pixelated Nanocapacitor Biosensor Platform for High-frequency Impedance Spectroscopy and Imaging," *IEEE Transactions on Biomedical Circuits and Systems* 12, no. 6 (2018): 1369–1382, https://doi.org/10.1109/TBCAS.2018.2861558.

38. C. Renault, C. Laborde, A. Cossettini, L. Selmi, F. Widdershoven, and S. G. Lemay, "Electrochemical Characterization of Individual Oil Microdroplets by High-frequency Nanocapacitor Array Imaging," *Faraday Discussions* 233 (2022): 175–189, https://doi.org/10.1039/D1FD00044F.

21983844, 0, Downloaded from https://advanced.onlinelibrary.wiley.com/doi/10.1002/advs.76880 by Jake Dales - Technical University Delft , Wiley Online Library on [03/08/2026]. See the Terms and Conditions (https://onlinelibrary.wiley.com/terms-and-conditions) on Wiley Online Library for rules of use; OA articles are governed by the applicable Creative Commons License

39. F. Widdershoven, "Pixelated Capacitive Sensors (PCS) for Embedded Multi-Sensing," in *Imaging Sensors, Power Management, PLLs and Frequency Synthesizers: Advances in Analog Circuit Design 2023* (Cham: Springer Nature Switzerland, 2024), 23–35.

40. P. Lenard and S. Saeland, "Über die Lichtelektrische und Aktinodielektrische Wirkung bei den Erdalkaliphosphoren," *Annalen der Physik* 333, no. 3 (1909): 476–502, https://doi.org/10.1002/andp.19093330303.

41. P. K. C. Pillai and R. Nath, "Photodielectric Effect in Photoconductors," *Physica Status Solidi (a)* 37, no. 2 (1976): 491–498, https://doi.org/10.1002/pssa.2210370217.

42. V. T. Avanesyan, G. A. Bordovskii, and S. A. Potachov, "Photodielectric effect," in *Wiley Encyclopedia of Electrical and Electronics Engineering* (2001), John Wiley & Sons Inc., https://doi.org/10.1002/047134608X.W6027.

43. H. Yang, J. Sun, Z. Uddin, et al., "Observation of Photodielectric Effect in Aluminum Nitride Piezoelectric Films," *ACS Applied Electronic Materials* 6, no. 5 (2024): 3422–3430, https://doi.org/10.1021/acsaelm.4c00222.

44. T. Nagai, K. Tanabe, I. Terasaki, and H. Taniguchi, "Systematic Tuning of the Photo-Dielectric Effect in $Ba(Al_{1-x}Zn_x)_2O_{4-\delta}$," *Applied Physics Letters* 113, no. 21 (2018), 212902, https://doi.org/10.1063/1.5036982.

45. M. Iwamoto, "Maxwell–wagner effect," in *Encyclopedia of nanotechnology* (Springer, 2015), 1–13.

46. S. V. Bhat, S. R. C. Vivekchand, A. Govindaraj, and C. N. R. Rao, "Photoluminescence and Photoconducting Properties of ZnO nanoparticles," *Solid State Communications* 149, no. 13–14 (2009): 510–514, https://doi.org/10.1016/j.ssc.2009.01.014.

47. F. Cao, Y. Liu, M. Liu, et al., "Wide Bandgap Semiconductors for Ultraviolet Photodetectors: Approaches, Applications, and Prospects," *Research* 7 (2024): 0385, https://doi.org/10.34133/research.0385.

48. D. Lohse, "Fundamental Fluid Dynamics Challenges in Inkjet Printing," *Annual Review of Fluid Mechanics* 54, no. 1 (2022): 349–382, https://doi.org/10.1146/annurev-fluid-022321-114001.

49. S. Santra, G. Hu, R. C. T. Howe, et al., "CMOS Integration of Inkjet-printed Graphene for Humidity Sensing," *Scientific Reports* 5, no. 1 (2015): 17374, https://doi.org/10.1038/srep17374.

50. T.-C. Wu, A. De Luca, Q. Zhong, et al., "Inkjet-printed CMOS-integrated Graphene–metal Oxide Sensors for Breath Analysis," *npj 2D Materials and Applications* 3, no. 1 (2019): 42, https://doi.org/10.1038/s41699-019-0125-3.

Supporting Information

Additional supporting information can be found online in the Supporting Information section.

Supporting File: advs76880-sup-0001-SuppMat.docx.

21983844, 0, Downloaded from https://advanced.onlinelibrary.wiley.com/doi/10.1002/advs.76880 by Joke Dales - Technical University Delft , Wiley Online Library on [03/08/2026]. See the Terms and Conditions (https://onlinelibrary.wiley.com/terms-and-conditions) on Wiley Online Library for rules of use; OA articles are governed by the applicable Creative Commons License